IEEE TRANSACTIONS ON POWER ELECTRONICS, VOL. 40, NO. 10, OCTOBER 2025 15959

Novel Integrated Optimization to Enhance Output Stability and Power Capability in EV Dynamic Wireless Charging Under Lateral Misalignment

Ke Shi, *Member, IEEE*, Chunsen Tang, *Member, IEEE*, Tianxu Feng, *Member, IEEE*, Peiyue Wang, Jincheng Jiang, Jun Wang, Jie Hou, *Member, IEEE*, and Shuaiyong Li, *Senior Member, IEEE*

***Abstract*—This article proposes a method to address the critical challenges of output fluctuation in electric vehicle dynamic wireless charging systems caused by transmitting coil switching under lateral misalignment. The main contributions include the bilateral reverse integrated magnetic coupler and the quasi-resonant *LCC* topology parameter optimization. Using the mutual inductance fluctuation ratio as a key indicator, the bilateral reverse coil is integrated and optimized to ensure stable output power during the transmitting coil switching under various lateral misalignments. An equivalent circuit model featuring a variable resistive load is developed to enhance output power capability while maintaining optimal weak inductive zero-voltage switching conditions. The integrated inductor broadens the selection of circuit parameters corresponding to the quasi-resonant range and reduces the parameter sensitivity. The method effectively maintains stable power output during transmitting coil switching under lateral misalignments, addressing cost, heat dissipation, and parameter deviation issues. A 4.5-kW prototype system is presented, and the simulation and experimental results demonstrate that it maintains stable power output within a 10-cm lateral misalignment range. Under $y = 0$ cm, 5 cm, and 10 cm, the output power fluctuation rates are ±4%, ±5%, and ±6%, respectively. The efficiency is above 91.5% .**

***Index Terms*—Electric vehicles dynamic wireless charging (EVDWC), lateral misalignment, *LCC–LCC* topology, magnetic integrated coupler, output stability, quasi-resonant parameters.**

Received 16 January 2025; revised 26 March 2025 and 12 May 2025; accepted 9 June 2025. Date of publication 12 June 2025; date of current version 5 August 2025. This work was supported in part by the National Key Research and Development Program of China under Grant 2022YFB3304500, in part by the Municipal Education Commission Science and Technology Research Plan Project of Chongqing under Grant KJQN202400626 and Grant KJZD-M202300605, in part by the National Natural Science Foundation of China under Grant 52277002, Grant 52307004, and Grant 62373070, in part by the Key Project of Chongqing Technological Innovation and Application Development under Grant CSTB2024TIAD-KPX0073, and in part by the Natural Science Foundation Joint Fund for Innovation and Development of Chongqing under Grant CSTB2024NSCQ-LZX0035. Recommended for publication by Associate Editor S. Mekhilef. *(Corresponding author: Ke Shi.)*

Ke Shi, Tianxu Feng, Peiyue Wang, Jincheng Jiang, Jun Wang, Jie Hou, and Shuaiyong Li are with the School of Automation, Chongqing University of Posts and Telecommunications, Chongqing 400065, China (e-mail: shike@cqupt.edu.cn; fengtx@cqupt.edu.cn; wangpy@cqupt.edu.cn; jiangjinc@cqupt.edu.cn; junwang@cqupt.edu.cn; houjie@cqupt.edu.cn; lishuaiyong@cqupt.edu.cn).

Chunsen Tang is with the School of Automation, Chongqing University, Chongqing 400000, China (e-mail: cstang@cqu.edu.cn).

Color versions of one or more figures in this article are available at https://doi.org/10.1109/TPEL.2025.3579343.

Digital Object Identifier 10.1109/TPEL.2025.3579343

NOMENCLATURE

h, h_s, h_e, h’	Detuning ratio coefficient.
λ	Power regulation coefficient.
$f(h)_{\max}$	Maximum resonant angle tangent value.
α, β	Resonant angle.
q	Expected maximum resonant offset.
p	Expected power regulation coefficient.
k_s	Coupling coefficient.
d	Air gap.
s	Gap distance.
y	Lateral misalignment distance.
g	Lower limit of the detuning ratio coefficient.
γ	Expected standard deviation of output.
δ	Standard deviation of output.
L_{p1}, L_{p2}, L_s	Transmitting coils and receiving coil.
L_{r1}, L_{r2}	Integrated bilateral reverse coils.
L_v	Secondary-side integrated inductor coil.
ω	Operating angular frequency.
$\boldsymbol{U}_{\text{dc}}, \boldsymbol{U}_d$	DC input voltage and battery voltage.
$\boldsymbol{Ui}, \boldsymbol{Uo}$	Equivalent input voltage and output voltage.
R	Equivalent variable resistance.
Z_{in}	Input impedance.
l_1, l_2, l_5	Sizes of the main coils.
l_3, l_4	Size of the integrated bilateral reverse coil.
l_6	Side length of the integrated inductor coil.
n_{w1}, n_{w2}	Turns of the main coils.
n_{w3}	Turns of the integrated bilateral reverse coil.
n_{w4}	Turns of the integrated inductor coil.
Δl	Step size for length optimization.
$C_1, C_{f1}, C_{p1}, C_2,$ C_{f2}, C_{p2}, C_s, C_v	Compensation capacitors.
$M_{pirj(i=1,2,j=1,2)},$ $M_{p1s}, M_{p2s}, M_{p1v},$ $M_{p2v}, M_{r1s}, M_{r2s},$ M_{r1v}, M_{r2v}, M_{sv}	Mutual inductances between the coils.
$\boldsymbol{I}_{p1}, \boldsymbol{I}_{p2}, \boldsymbol{I}_1, \boldsymbol{I}_2,$ $\boldsymbol{I}_3, \boldsymbol{I}_s, \boldsymbol{I}_{\text{in}}$	Currents in circuit.

$L_a, L_b, L_{se}, L_{ses}$, L_{f1}, L_{f2}	Equivalent self-inductance value.
M_{s1}, M_{s2}, M_s, M_{v1}, M_{v2}, M_v	Equivalent mutual inductance.
$M_{v\max}$	Maximum value of cross mutual inductance.
$M_{s\cdot 0}$	Mutual inductance at the transition center.
$M_{s\cdot 1}$	Mutual inductance at center of a coil.
$M_{s\cdot 2}$	Mutual inductance at one-quarter of a coil.
$R_m (m = 1, \ldots, 9)$	Internal resistances.
P_{outh1}	Output power under the detuning ratio coefficient parameter configuration.
P_{out1}	Output power under complete resonance.

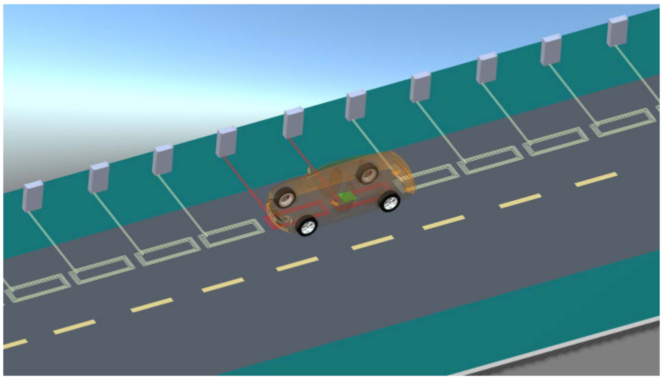

Fig. 1. EVDWC system with a segmented rail layout.

I. INTRODUCTION

With the rapid growth of electric vehicles (EVs), the conventional wired charging method is encountering significant issues, such as cumbersome operations, exposed wires, and potential leakage risks. Wireless charging technology has emerged as a crucial solution. This technology uses spatial electromagnetic fields from high-frequency currents for power transmission. It has been preliminarily implemented for static power supply in fixed parking spaces. However, issues, such as range anxiety, charging queues, and high land occupancy rates, still persist. Electric vehicle dynamic wireless charging (EVDWC) technology allows a seamless, real-time power supply to moving vehicles via embedded transmitting coils in the road [1], [2], [3]. This significantly reduces battery capacity requirements and extends driving range.

In the EVDWC system, the layout of the segmented rail reduces no-load losses and electromagnetic radiation while improving coupling coefficients [4], as illustrated in Fig. 1. During vehicle operation, the relative movement between the receiving coil and the segmented transmitting arrays inevitably leads to disturbances from electromagnetic coupling. These disturbances appear as variations in mutual inductance, which can destabilize the power transmission characteristics and result in output fluctuation [5]. The instability poses potential risks to the lifespan of the power battery and may compromise driving safety [6].

Recent research on the power stability of EVDWC systems primarily investigated fluctuation caused by transmitting coil switching. These studies mainly focused on four key aspects: magnetic coupler design, control strategies, topology parameters optimization, and magnetic integrated method. The magnetic coupler design method emphasizes the design, arrangement, magnetic core configuration, and winding technique of coupled coils to enhance the distribution of excitation magnetic fields [7], [8], [9], [10]. Although these methods have good effects, their universality and compatibility in design are insufficient. The use of control strategies [11], [12], [13], [14] or multiphase excitation [15], [16], [17] is also a common method to address output power fluctuation. Although the feasibility of the control strategy discussed in the aforementioned papers has been established, the rapid movement of the pickup poses challenges for implementing and applying the control strategy effectively. Improving the tolerance of compensation network parameters or impedance matching has been shown to optimize the stable output power [18], [19]. These methods have high feasibility, but the power fluctuation suppression effect is still limited. The magnetic integrated method is a novel solution that addresses power stability issues in EVDWC systems. Methods for suppressing power fluctuation using a magnetic integrated coupler have been proposed, achieving stable output power performance without additional control during normal system operation [20], [21].

In summary, a series of studies have been conducted on suppressing output power fluctuation caused by transmitting coil switching. However, traditional methods fail to address output power fluctuation in EVDWC systems caused by simultaneous lateral misalignment and transmitting coil switching. Therefore, the issue of output power fluctuation in EVDWC systems under lateral misalignment still needs to be urgently addressed.

This article proposes a novel magnetic integrated method and quasi-resonant parameter optimization to address the issue. A bilateral reverse integrated (BRI) magnetic coupler is presented, and the optimization of bilateral reverse coils is explored to achieve stable power output during the transmitting coil switching process under varying lateral misalignments. Furthermore, a quasi-resonant parameter optimization method for the EVDWC system with *LCC–LCC* topology is proposed based on the equivalent circuit model of a variable resistive load. The mechanism of the variable resistive model for *LCC–LCC* topology under a nonresonant parameter configuration is revealed. Detailed quasi-resonant parameters and coupler optimization design process have been provided. And the detuning circuit parameter selection corresponding to the quasi-resonant range is broadened by the secondary-side magnetic integration. The effect of enhancing output power capability through a single parameter while maintaining zero-voltage switching (ZVS) operation is achieved. By minimizing output power fluctuation during transmitting coil switching under lateral misalignment and compensating for power drops caused by lateral misalignment, the power stability is achieved while accommodating various lateral misalignments. The main contributions of this article are summarized as follows:

1) *Propose a new magnetic coupler*: A BRI magnetic coupler is proposed, and stable output power along the EV moving

direction under lateral misalignment is achieved through detailed optimization.

2) *Propose novel quasi-resonant optimization*: The parameter optimization method for quasi-resonant *LCC–LCC* topology is proposed using a variable resistance load model under the battery voltage constraint condition, achieving its output power capability improvement while maintaining an optimal weak inductive ZVS condition.
3) *Present detailed design process*: The flowchart for optimizing the parameters of the EVDWC system is presented, facilitating the step-by-step customization of resonance conditions, output performance, and parameter robustness to meet practical requirements.

II. SYSTEM CONFIGURATION AND FEATURE ANALYSIS

A. *BRI Magnetic Coupler*

The short rail structure is a layout where the size of the transmitting coil and the receiving coil is similar, which comprehensively considers the length of the EV and the energy utilization rate. When the receiving coil moves along the transmitting coils, the transmitting coils below the EV are activated and turned OFF in turn. In the working area accompanied by the EV, only the two transmitting coils are activated, while the outer coils on both sides are not activated. This feature corresponds to its less energy waste and lower electromagnetic leakage characteristics. From a structural point of view, the analysis of two adjacent transmitting coils is sufficient for all working conditions and can verify the working principle of the proposed method.

The power fluctuation and reduced output capability of the EVDWC system under lateral misalignment are mainly caused by changes in mutual inductance between the transmitting and receiving coils. This article proposes a BRI magnetic coupler, achieving output stability and power enhancement under lateral misalignment from two aspects: intrinsic magnetic field adaptation and magnetic coupling parameter regulation. By integrating a bilateral reverse coil at the transmitter, the original single coupling is replaced by the equivalent mutual inductance difference, altering the dynamic coupling characteristics without changing the original magnetic coupler. For magnetic coupling parameter regulation, a quasi-resonant parameter optimization method using variable resistance for battery load modeling in *LCC* topology is proposed. A compensation inductor in the secondary-side *LCC* network is also integrated into the coupler, which expands the selection of circuit parameters corresponding to the quasi-resonant range. Based on the composite parameter optimization with the novel magnetic coupler, a wide range of output power regulation capabilities can be achieved while maintaining ZVS operation. The integrated optimization can effectively suppress output power fluctuation under lateral misalignment to ensure the power output required by the system and also make the system more compact.

The proposed BRI magnetic coupler is presented in Fig. 2. It comprises three modules, including two identical transmitters and one receiver. The transmitter consists of a magnetic core plate and two coils, and the receiver consists of a magnetic core plate, a shielding plate, and two coils. Within the coils of the coupler, L_{p1} and L_{p2} are the two adjacent transmitting coils, while L_{r1} and L_{r2} are the corresponding integrated bilateral reverse coils. L_s is the receiving coil, and L_v is the secondary-side integrated inductor coil. The connection sequence between the main coils and the integrated coils and their winding directions are shown in Fig. 3.

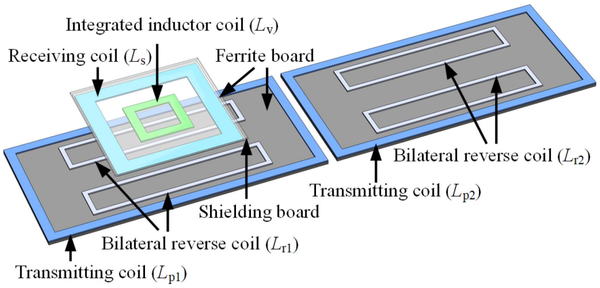

Fig. 2. Proposed BRI magnetic coupler.

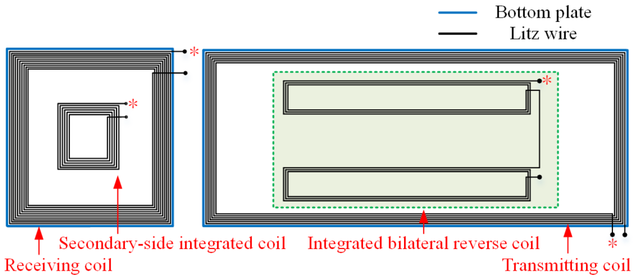

Fig. 3. Connection sequence between the main coils and the integrated bilateral reverse coils and their winding directions.

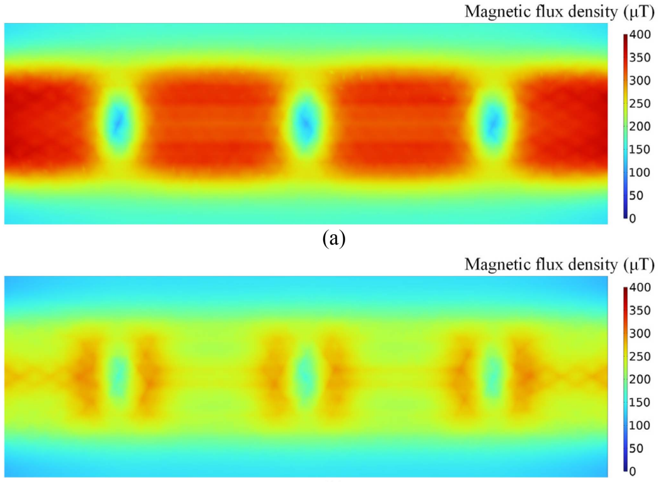

(a)

(b)

Fig. 4. Comparison of magnetic flux density distribution. (a) With the conventional single-pole coil structure. (b) With the proposed BRI magnetic coupler.

The comparison of magnetic flux density distribution between the BRI magnetic coupler and conventional single-pole coil structure is shown in Fig. 4. It indicates that the integrated bilateral reverse coils effectively shape the excited magnetic field, ensuring that the magnetic field lines passing through the

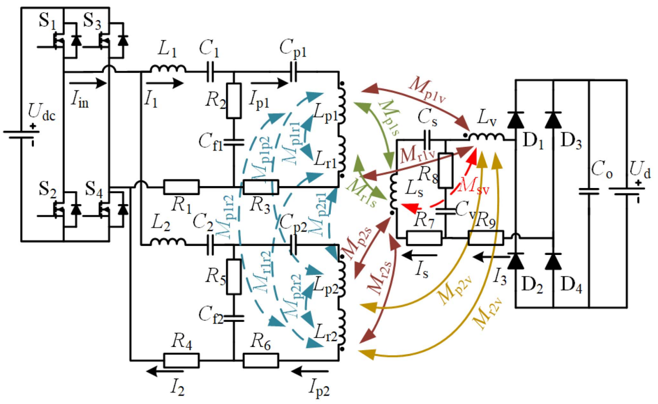

Fig. 5. Circuit of the EVDWC system with magnetic integrated design.

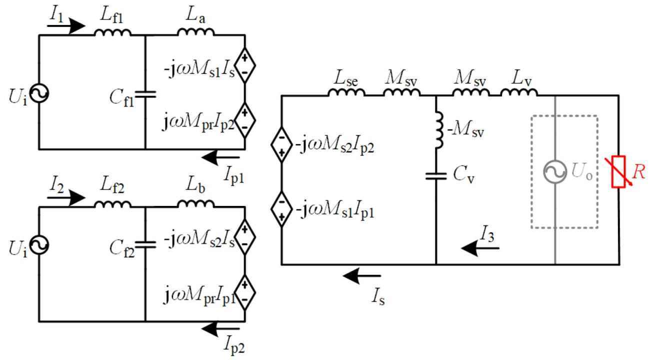

Fig. 6. Equivalent topology with equivalent variable resistance load.

receiving coil remain stable during vehicle movement. Under a certain lateral misalignment condition, this optimization effect is still effective along the direction of EV movement.

B. *Circuit Modeling of the Quasi-Resonant* LCC *Topology*

To reveal the output characteristics through mathematical expressions, a fundamental harmonic approximation analysis method is employed, neglecting the power losses of the components. The circuit diagram of the EVDWC system with BRI magnetic coupler is shown in Fig. 5. The two transmitters are identical and connected in parallel, sharing a full-bridge inverter. S_1–S_4 are the primary-side power MOSFETs, forming a full-bridge inverter, and D_1–D_4 are the secondary-side diodes, forming the rectification circuit. Coils L_{p1} and L_{r1} are connected in reverse series as the first transmitter, while coils L_{p2} and L_{r2} are connected in series as the second transmitter. Coils L_s and L_v form the receiver. L_1 and L_2 are the compensated inductors in the *LCC* resonant network on the primary side. C_1, C_2, C_{f1}, C_{f2}, C_{p1}, C_{p2}, C_s, and C_v are the compensated capacitors. C_o is the filtering capacitor. M_{p1r2}, M_{p1p2}, M_{r1r2}, M_{p1r1}, M_{p2r1}, and M_{p2r2} are the mutual inductances among the primary-side coils, which are typically fixed constants; thus, approximate decoupling can be achieved through the parameter design of compensation capacitors. M_{p1v}, M_{r1v}, M_{p2v}, M_{r2v}, M_{p1s}, M_{r1s}, M_{p2s}, and M_{r2s} are the cross couplings among the secondary-side coils and the primary-side coils. M_{sv} is the mutual inductance between the receiving coil and the integrated inductor coil. $R_m (m = 1, 2,, \ldots, 9)$ indicates the internal resistances of the components. $\boldsymbol{U}_{\mathrm{dc}}$ and $\boldsymbol{U}_d$ are the dc input voltage and the load output voltage, respectively. $\boldsymbol{U}_i$ and $\boldsymbol{U}_o$ are the equivalent ac input voltage and load output voltage, respectively. $\boldsymbol{I}_{p1}$ and $\boldsymbol{I}_{p2}$ are the currents of the transmitting coils, and $\boldsymbol{I}_s$ is the current of the reception coil. $\boldsymbol{I}_{\mathrm{in}}$ is the total inverter output current. $\boldsymbol{I}_1$ and $\boldsymbol{I}_2$ are the inverter output branch currents corresponding to the two transmitters, and $\boldsymbol{I}_3$ is the equivalent load output current. The system operates at a frequency *f*, with angular frequency $\omega = 2\pi f$.

Internal resistances are ignored in the analysis process to obtain more meaningful expressions by solving mathematical models. In Section IV, the impact of internal resistances on the system is verified through simulation and experiments. The equivalent circuit topology of the EVDWC system with a variable resistive load model is presented in Fig. 6. To simplify the expression of the equation, the following mutual inductances are defined:

$$\begin{aligned} M_{v1} &= M_{p1v} - M_{r1v}, \quad M_{s1} = M_{p1s} - M_{r1s} \\ M_{v2} &= M_{p2v} - M_{r2v}, \quad M_{s2} = M_{p2s} - M_{r2s} \\ M_{pr} &= M_{p1p2} + M_{r1r2} - M_{p1r2} - M_{p2r1}. \end{aligned} \tag{1}$$

M_{v1} and M_{v2} represent the mutual inductance differences between the secondary-side integrated inductor coil and the primary coils. The facing area between the secondary-side inductor coil and the bilateral integrated reverse coil can be much smaller compared with the receiving coil. And the turns of the secondary-side inductor coil can be settled much smaller than that of the receiving coil. Based on the mutual inductance calculation formula, M_{v1} and M_{v2} can be easily designed to be much smaller than M_{s1} and M_{s2}. Therefore, to obtain a more meaningful expression, M_{v1} and M_{v2} are neglected in theoretical analysis. M_{p1r1} and M_{p2r2} are the internal mutual inductances directly connected in series within the circuit and are typically fixed values. Therefore, they can be equivalently considered as a part of the circuit elements as follows:

$$\begin{aligned} L_a &= L_{p1} + L_{r1} - 1/(\omega^2 C_{p1}) - 2M_{p1r1} \\ L_b &= L_{p2} + L_{r2} - 1/(\omega^2 C_{p2}) - 2M_{p2r2} \\ L_{se} &= L_s - 1/(\omega^2 C_s). \end{aligned} \tag{2}$$

At the receiver, the internal mutual inductance between the receiving coil and the integrated inductor coil can be decoupled through an equivalent T-type network. The T-type network introduced by M_{sv} is expected to alter the impedance of the secondary-side circuit without affecting the resonant state, thereby providing a means to enhance the output power. L_{f1} and L_{f2} represent the inductors in the series branch as follows:

$$L_{f1} = L_1 - 1/(\omega^2 C_1), \quad L_{f2} = L_2 - 1/(\omega^2 C_2). \tag{3}$$

The compensate capacitor C_v is set as the detuning factor, and the detuning ratio coefficient is defined as *h*. The resonant network parameters are configured as follows:

$$\begin{aligned}&L_{ses}=L_{se}+M_{sv},\quad L_{sv}=L_{v}+M_{sv}\\&\omega^2L_{f1}C_{f1}=\omega^2L_{f2}C_{f2}=1\\&\omega^2(L_a+M_{pr})C_{f1}=\omega^2(L_b+M_{pr})C_{f2}=1\\&h\omega^2L_{ses}C_v=h\omega^2L_{sv}C_v=1+\omega^2M_{sv}C_v.\end{aligned}\tag{4}$$

Furthermore, according to (2), $L_a = L_{f1}$ and $L_b = L_{f2}$ can be achieved by configuring C_{p1} and C_{p2}. Considering the consistency of parameters between adjacent transmitters, the equivalent inductor parameters are configured as follows:

$$L_{f1}=L_{f2}=L_f.\tag{5}$$

The cross coupling is simplified to be described as follows:

$$M_s=M_{s1}+M_{s2}.\tag{6}$$

The voltage across the battery load has a certain range and does not change abruptly during the charging process. For high-frequency EVDWC systems, this can be considered as a constant voltage value. Due to the characteristics of the rectifier, its voltage and current are approximately in phase. Therefore, the battery load can be equivalently represented as a variable resistor that satisfies the following constraints:

$$\left|\dot{U}_o\right|=\left|\dot{I}_3\right|R.\tag{7}$$

The KCL equations for the system are given, as shown in (8) shown at the bottom of this page. The values of the currents in the transmitting coils and the output current are calculated as follows:

$$\begin{cases}\dot{I}_{p1}=-\frac{j\dot{U}_i}{\omega L_f}\\\dot{I}_{p2}=-\frac{j\dot{U}_i}{\omega L_f}\\\dot{I}_3=\frac{hM_s\dot{U}_i}{(h-1)L_fR+j(2h-1)\omega L_fL_{ses}}.\end{cases}\tag{9}$$

According to (9), the current of the transmitting coil is independent of the load, thus achieving a constant current output characteristic. The magnitude of the output current is expressed as follows:

$$\left|\dot{I}_3\right|=\frac{hM_s\left|\dot{U}_i\right|}{L_f\sqrt{(1-h)^2R^2+(1-2h)^2\omega^2{L_{ses}}^2}}.\tag{10}$$

Combining (7) and (10), the load equivalent variable resistance can be expressed as follows:

$$R=\frac{(-1+2h)\,\omega L_fL_{ses}\left|\dot{U}_o\right|}{\sqrt{\left|-h^2{M_s}^2\left|\dot{U}_i\right|^2+(h^2-2h+1){L_f}^2\left|\dot{U}_o\right|^2\right|}}.\tag{11}$$

From (10) and (11), the output current is re-expressed as follows:

$$\left|\dot{I}_3\right|=\frac{hM\left|\dot{U}_i\right|}{|2h-1|\,\omega L_fL_{ses}\sqrt{1+\frac{1}{\left|1-\frac{h^2}{(h-1)^2}\frac{{M_s}^2|\dot{U}_i|^2}{L^2{}_f|\dot{U}_o|^2}\right|}}}.\tag{12}$$

The total input equivalent impedance of the system is given as follows:

$$Z_{\text{in}}=\frac{\dot{U}_i}{\dot{I}_1+\dot{I}_2}.\tag{13}$$

Combining (8), (11), and (13), the tangent of the resonant angle is solved, as shown in the following equation: (14) shown at the bottom of this page,*f*(*h*) passes through the fixed point (1, 0). And there are two boundary lines $k_1 = L_f|\boldsymbol{U}_\mathbf{o}|/(L_f|\boldsymbol{U}_\mathbf{o}| + M_s|\boldsymbol{U}_\mathbf{i}|)$ and $k_2 = L_f|\boldsymbol{U}_\mathbf{o}||/(L_f|\boldsymbol{U}_\mathbf{o}|-M_s|\boldsymbol{U}_\mathbf{i}|)$, which cause the function to segment at $h = k_1$ and $h = k_2$. By optimizing the system parameter L_f, a small function value close to 0 can be achieved within the range (k_1,1).

The positive and negative values of *f*(*h*) represent the inductive and capacitive operating states, respectively. Therefore, based on the maximum offset requirement relative to the resonant state, a weakly inductive ZVS operating state can be achieved within the range (h_1,1). Furthermore, the maximum resonant angle tangent value of the total equivalent impedance within this range

---

$$\begin{bmatrix}0&j\omega L_{f1}&0&0&0&0\\j\omega L_f&0&0&0&-j\omega M_{s1}&0\\0&0&0&j\omega L_f&0&0\\0&0&j\omega L_f&0&-j\omega M_{s2}&0\\0&-j\omega M_{s1}&0&-j\omega M_{s2}&j\omega(1-h)L_{ses}&j\omega hL_{ses}\\0&0&0&0&j\omega hL_{ses}&j\omega(1-h)L_{ses}+R\end{bmatrix}\begin{bmatrix}\dot{I}_1\\\dot{I}_{p1}\\\dot{I}_2\\\dot{I}_{p2}\\\dot{I}_s\\\dot{I}_3\end{bmatrix}=\begin{bmatrix}\dot{U}_i\\0\\\dot{U}_i\\0\\0\\0\end{bmatrix}.\tag{8}$$

$$\tan\alpha=\frac{\text{Im}[Z_{\text{in}}]}{\text{Re}[Z_{\text{in}}]}=f(h)=\frac{(h-1)\left((1-2h){L_f}^2\left|\dot{U}_o\right|^2+\left|h^2{M_s}^2\left|\dot{U}_i\right|^2-(h-1)^2{L_f}^2\left|\dot{U}_o\right|^2\right|\right)}{h^2L_f\left|\dot{U}_o\right|\sqrt{\left|h^2{M_s}^2\left|\dot{U}_i\right|^2-(h-1)^2{L_f}^2\left|\dot{U}_o\right|^2\right|}}.\tag{14}$$

is calculated as follows:

$$f(h)_{\max} = \frac{(h_1 - 1)\left(M_s{}^2\left|\dot{U}_i\right|^2 - L_f{}^2\left|\dot{U}_o\right|^2\right)}{L_f\left|\dot{U}_o\right|\sqrt{h_1{}^2 M_s{}^2\left|\dot{U}_i\right|^2 - (h_1 - 1)^2 L_f{}^2\left|\dot{U}_o\right|^2}}. \tag{15}$$

According to (15), after the standard input and output voltages are determined, $f(h)_{\max}$ is a functional expression under the joint action of variables h_1, L_f, and M_s. The output power calculated from (11) and (12) is expressed as in (16) shown at the bottom of this page. The output power under resonance is denoted as P_{out1}, and the output power under the detuning ratio coefficient parameter configuration is denoted as P_{outh1}. The power regulation coefficient is defined as λ

$$\lambda = \frac{P_{\text{outh1}} - P_{\text{out1}}}{P_{\text{out1}}} \times 100\%. \tag{17}$$

C. Output Performance Analysis

Based on the predetermined mutual inductance M_s, the lower limit h_1 of the detuning ratio coefficient range can be determined by targeting the maximum resonant angle tangent value $f(h)_{\max}$ and the power regulation coefficient λ based on (15) and (17). The range $(h_1, 1)$ is defined as the quasi-resonant parameter range. Based on the mathematical analysis of (12), the sensitivity of output current to h is relatively small. And it is possible to achieve an approximately constant current output characteristic through appropriate parameter settings. By designing a small $f(h)_{\max}$ close to zero, as indicated by (15), the entire quasi-resonant range can be ensured to operate in a weakly inductive ZVS state. Within this range, different values of h correspond to different output powers, providing a novel approach to power regulation. Furthermore, based on (14), it is known that changes in output voltage can affect the resonant state. Considering the limitations of the battery charging voltage range, the impact of different output voltages on the tangent of the resonant angle within a specific range is relatively minor, which can be mitigated through parameter adjustments.

To address the issue of output power fluctuation in EVDWC system considering lateral misalignment, the total equivalent mutual inductance M_s is first optimized based on the bilateral reverse coil magnetic integration. This optimization enhances the stability during the EV movement process under lateral misalignments. Then, taking the mutual inductance M_{s0}, M_{s1}, … under different lateral misalignments as inputs and targeting the maximum resonant offset angle and the power regulation coefficient, the quasi-resonant parameters are optimized.

D. Detuning Circuit Parameter Range Analysis

Integrating the secondary-side compensation inductor into the receiver can improve the coupler compactness [22], the output power capacity [23], and the heat dissipation ability [24]. In this article, an integrated inductor coil also contributes to broadening the selection of circuit parameters corresponding to the quasi-resonant range, thereby reducing the quasi-resonant circuit parameter sensitivity and improving the fault tolerance.

The core function of integrating L_v is to introduce the internal mutual inductance M_{sv} into the secondary-side LCC resonant network. Without the effect of M_{sv}, the parameter h' is represented as follows:

$$h' = \frac{1}{C_v} \cdot \frac{1}{\omega^2 L_v}. \tag{18}$$

With the effect of M_{sv}, the parameter h is represented as

$$h = \frac{M_{sv}}{L_v + M_{sv}} + \frac{1}{C_v} \cdot \frac{1}{\omega^2 (L_v + M_{sv})}. \tag{19}$$

C_v is the circuit parameter used to configure the quasi-resonant state. According to (18) and (19), two characteristics from M_{sv} can be obtained as follows: First, the selection of circuit parameters C_v corresponding to the quasi-resonant range is broadened. Parameters h and h' are both proportional functions of $1/C_v$. In (19), the proportionality coefficient is $1/[\omega^2(L_v + M_{sv})]$, which is smaller than $1/(\omega^2 L_v)$ in (18). Therefore, h has a smaller change rate along with the change of C_v. The parameter sensitivity is greatly reduced and the fault tolerance rate is improved. Second, a fixed lower limit of detuning ratio coefficient is introduced, which can be used as a design index to configure the range of the detuning circuit parameter. In both (18) and (19), the detuning ratio coefficients are negatively correlated with C_v. Within the concerned h' range of (0, 1), as C_v increases, the lower limit of h' is zero. In contrast, the lower limit of h is $M_{sv}/(L_v + M_{sv})$, a positive value that can be configured through system parameters. The magnetic integration brings a detuning ratio coefficient lower limit, and the setting of the lower limit decides the degree of circuit parameters broadening.

In addition, the comparison between the circuit parameter C_v corresponding to the quasi-resonant range with and without magnetic integration is shown in Fig. 7. The capacitor under resonance is different because the total equivalent inductance in the two cases is configured equally to ensure the rationality of the comparison. The result shows that, within the same quasi-resonant detuning ratio coefficient range, the range of the corresponding detuning circuit parameter C_v is larger, which means that the parameter sensitivity is greatly reduced and the fault tolerance rate is improved. According to Fig. 7, the secondary-side integrated coil introduces a lower limit of the detuning ratio coefficient, which can be configured according to

$$P_{\text{out}} = \left|\dot{I}_3\right|^2 R = \frac{h^2 M_s{}^2\left|\dot{U}_i\right|^2\left|\dot{U}_o\right|\sqrt{\left|h^2 M_s{}^2\left|\dot{U}_i\right|^2 - (-1+h)^2 L_f{}^2\left|\dot{U}_o\right|^2\right|}}{(-1+2h)\,\omega L_f L_{ses}\left[(-1+h)^2 L_f{}^2\left|\dot{U}_o\right|^2 + \left|h^2 M_s{}^2\left|\dot{U}_i\right|^2 - (-1+h)^2 L_f{}^2\left|\dot{U}_o\right|^2\right|\right]}. \tag{16}$$

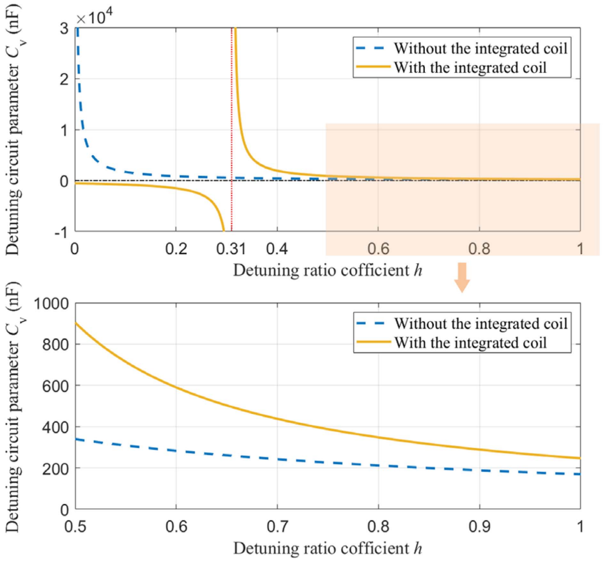

Fig. 7. Comparison of the circuit parameters corresponding to the quasi-resonant range with and without magnetic integration.

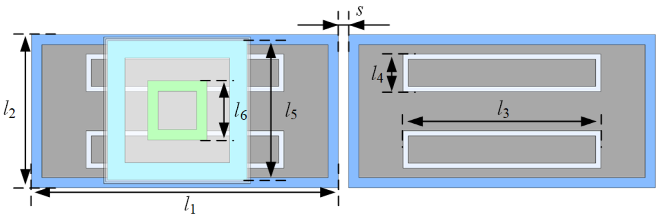

Fig. 8. Structure of the BRI magnetic coupler.

TABLE I
PARAMETERS OF THE BRI MAGNETIC COUPLER

Type	Parameter	Description	Value
Initial parameters	l_1	Length of $L_{p1}(L_{p2})$	90 cm
	l_2	Width of $L_{p1}(L_{p2})$	45 cm
	l_5	Side length of L_s	40 cm
	n_{w1}	Turns of $L_{p1}(L_{p2})$	6
	n_{w3}	Turns of L_s	10
	d	Air gap	15 cm
	s	Gap distance between two transmitting coils	3 cm
	x	Receiving coil position	–45 cm~45 cm
	y	Lateral misalignment distance	0 cm, 5 cm, 10 cm
Optimization parameters	l_3	Length of $L_{r1}(L_{r2})$	60 cm
	l_4	Width of $L_{r1}(L_{r2})$	11 cm
	l_6	Side length of L_v	16 cm
	n_{w2}	Turns of $L_{r1}(L_{r2})$	6
	n_{w4}	Turns of L_v	6

different practical needs. The lower limit can be used as a design index to configure the range of the detuning circuit parameter.

III. QUASI-RESONANT PARAMETERS OPTIMIZATION AND BRI MAGNETIC COUPLER DESIGN

A. Optimization and Design Process of the EVDWC System

The primary objective is to suppress the output power fluctuation during transmitting coil switching under lateral misalignment. The optimization and design process are primarily reflected in two aspects: First, smooth the total equivalent mutual inductance between the receiving and primary coils, ensuring stability as the receiving coil moves along the transmitting coils under various lateral misalignments. Second, optimize the circuit parameters based on the mutual inductance values at different lateral misalignments to enhance the robustness of the ZVS operating state and the power transfer capability.

In this article, the analysis method based on MAXWELL finite-element simulation software is used to optimize and design the EVDWC system, which is widely used in electromagnetic simulation research [25], [26]. The simulation adopts the magnetostatic solution type. The current modeling of the coil is based on the assumption of a continuous medium with equivalent body current density to achieve efficient simulation. The BRI magnetic coupler modeled using MAXWELL is shown in Fig. 8, and the parameters describing the dimensions of the coupler are defined in Table I. This article establishes a typical EVDWC system at a 4.5-kW power level to validate the design methodology.

The design process for the integrated bilateral reverse coil and quasi-resonant parameters is shown in Fig. 9. First, the initial parameters of the EVDWC system are selected, and the main coils are designed considering the coupling coefficient and practical application scenarios. Under the condition of no lateral misalignment and in the well-aligned state, the turns n_{w2} of the integrated bilateral reverse coil are determined based on the output power level and the initial turns n_{w1} of the transmitting coil. Second, the size parameters of the integrated bilateral reverse coil are optimized under lateral misalignments $y = 0$ cm, 5 cm, and 10 cm, respectively, to achieve a stable equivalent mutual inductance compatible with different lateral misalignments' states as the receiving coil moves along the transmitting coils. Three equivalent mutual inductances are analyzed to describe the fluctuation characteristics of power transmission: $M_{s'0}$ at the transition center position between the two transmitting coils, $M_{s'1}$ at the center of a single transmitting coil, and $M_{s'2}$ at the one-quarter of a single transmitting coil. The mutual inductance fluctuation ratio δ is defined as the standard deviation $\delta_i = \sigma(M_{s'0}, M_{s'1}, M_{s'2})$. Finally, based on the optimized mutual inductance derived from (15) and (17), the value of L_f is optimized, which further determines the quasi-resonant operating range $(h_1, 1)$.

In the design process, γ represents the expected standard deviation of power fluctuation and is the target input used to optimize M_s. q and p represent the expected maximum resonant offset angle and power regulation coefficient, respectively. These are the target inputs used to optimize and determine the quasi-resonant parameter range. In practical applications, the air gap distance, magnetic coupler size, magnetic core configuration, parameter sensitivity capability, and system design requirements may need different suitable detuning ratio coefficient configurations. To verify the feasibility of the proposed method, this article sets the power adjustment coefficient $p = 0.6$ and the maximum resonant angle tangent value offset $q = 0.2$. The target value for

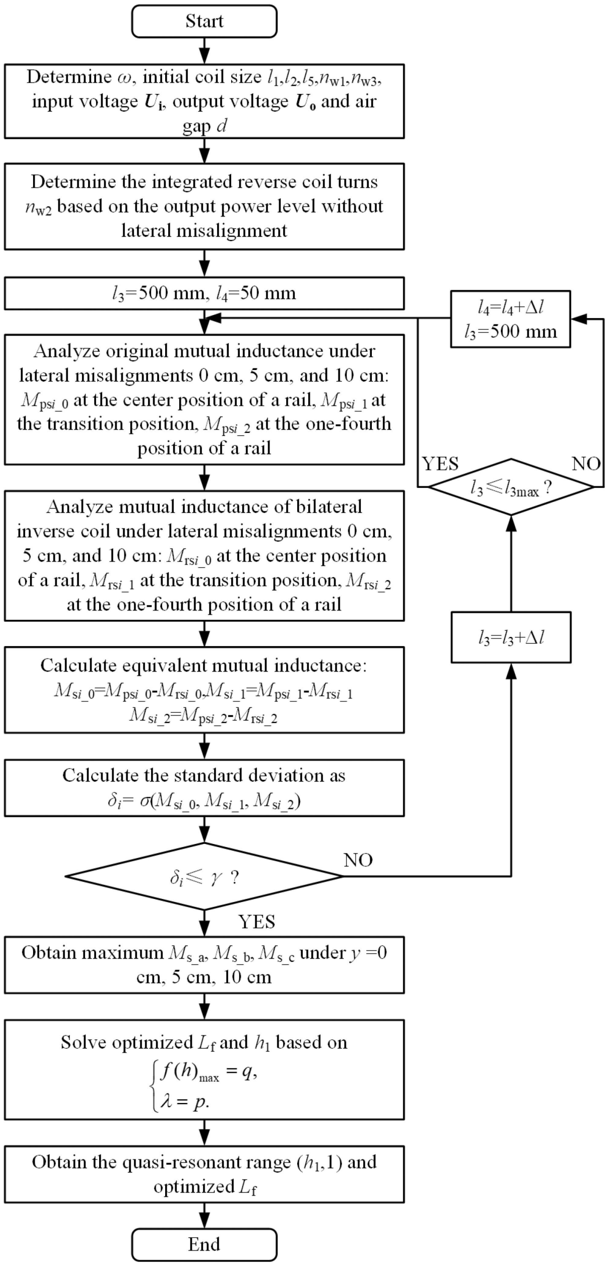

Fig. 9. Design process of the integrated bilateral reverse coil and quasi-resonant parameters.

the mutual inductance standard deviation is $\gamma = 0.5$. The step sizes for the length and width of the BRI coil are $\Delta l = 10$ mm, and the diameter of the Litz wire used is $a = 5$ mm.

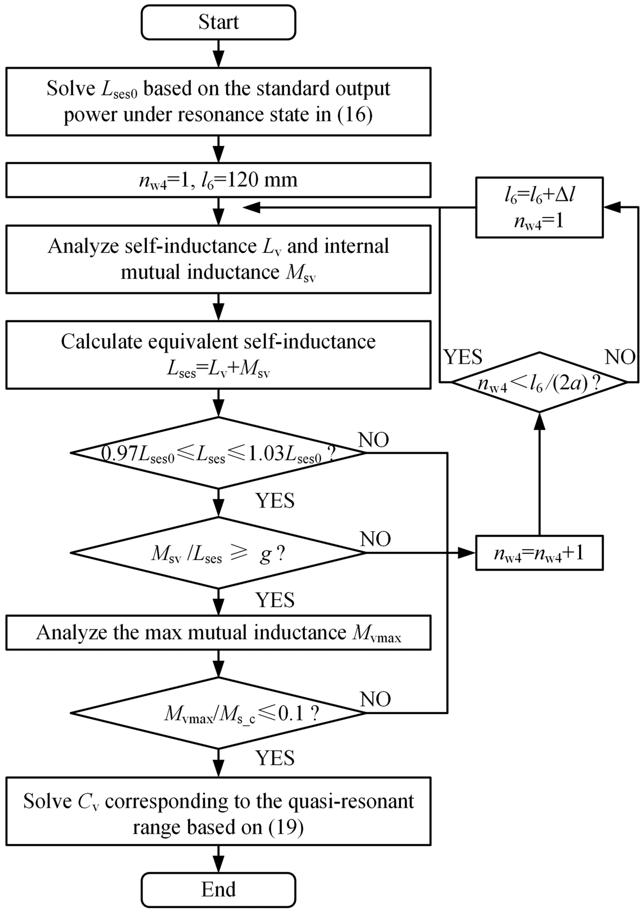

Fig. 10. Design process of secondary-side integrated inductor coil.

Following the completion of the integrated bilateral reverse coil and the quasi-resonant range design, further research is conducted on the secondary-side integrated inductor optimization to broaden the range of circuit parameters corresponding to the detuning ratio coefficient. The design process for the secondary-side integrated inductor coil is depicted in Fig. 10. First, L_{ses0} is solved based on the standard output power under resonance state. Second, with the value of L_{ses0} as the objective, the size of the integrated inductor coil is optimized under the joint constraints of the lower limit of the expected detuning ratio coefficient and the $M_{v\max}$ range. Finally, the detuning factor parameter C_v corresponding to the quasi-resonant range is solved based on (19). The lower limit of the detuning ratio coefficient is set to $g = 1/3$, and the step size for the integrated coil edge length is $\Delta l = 10$ mm.

B. Tested Initial Magnetic Coupler Configuration

In the verification system of this article, the size of the receiving coil is selected as "400 mm $*$ 400 mm $*$ 5 mm," and the turns n_{w3} is 10. Ferrite plates and aluminum shielding plates are used for magnetic field enhancement and electromagnetic shielding, respectively. The size of the secondary-side ferrite plate is "400 mm $*$ 400 mm $*$ 10 mm," the size of the aluminum shield is "420 mm $*$ 420 mm $*$ 5 mm," and the air gap is $d = 150$ mm. The size of the transmitting coil is designed as "900 mm $*$ 450 mm $*$ 5 mm," and the turns n_{w1} is designed as 6.

In the EVDWC system, the cross coupling between two adjacent transmitting coils causes the activated coil to be affected by nearby inactive coils. Excessive cross coupling makes it difficult to configure compensation capacitors in practical applications. Therefore, the gap distance *s* between two adjacent transmitting coils is optimized to avoid excessive cross coupling. The relationship between coupling coefficient k_s and gap distance *s* is

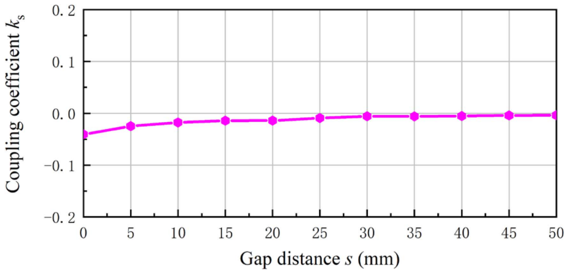

Fig. 11. Relationship between coupling coefficient k_s and gap distance s.

obtained, as shown in Fig. 11. The result shows that, after the gap distance reaches 30 mm, the value of k_s is negligible and decreases slowly. Therefore, setting the gap distance s to 30 mm is a reasonable choice, allowing for effective compensation of mutual coupling without significantly impacting the system.

C. Optimization of the Integrated Bilateral Reverse Coils and Quasi-Resonant Parameters

The integration of the bilateral reverse coil at the transmitter aims to optimize the coupling for power transmission. The challenge of mitigating output power fluctuation under lateral misalignment is transferred to stabilizing the mutual inductance difference between the receiving coil and the transmitting coils on the road. Consequently, it is imperative that the coupling characteristics of the integrated bilateral reverse coil and the receiving coil closely approximate those of the conventional transmitting coil and receiving coil. This similarity ensures that the superposition of the two mutual inductances results in a more stable configuration, optimizing the overall system performance during transmitting coil switching under lateral misalignment. The design parameters of the integrated bilateral reverse coil include the length l_3, width l_4, and the turns n_{w2}. The turns n_{w2} is set to 3 to ensure compatibility with a power level of 4.5 kW in the verification prototype.

Due to the size limitation of the outer transmitting coil, the length range of the integrated bilateral reverse coil located inside is set between 500 and 800 mm, while the width range is from 50 to 150 mm. Fig. 12 shows the optimization results of length and width dimensions with the objective of the expected mutual inductance difference ratio at different lateral displacement distances. A common value region of less than 0.5 is obtained from the three traversal results, as shown in Fig. 12, which minimizes the difference in mutual inductance among different lateral misalignment situations. The optimized results obtained within this area are a length of 600 mm and a width of 110 mm.

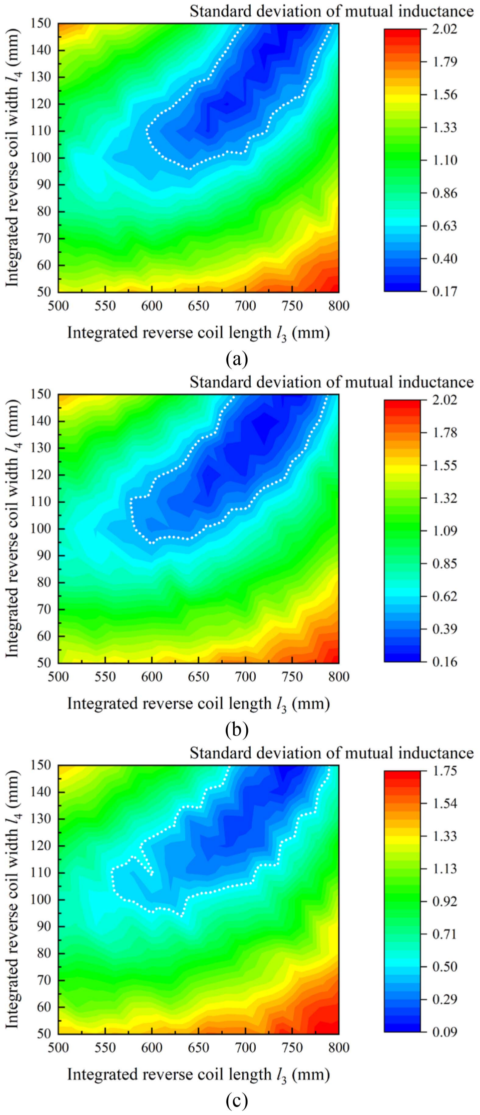

Fig. 12. Optimization results of bilateral reverse coil length and width dimensions. (a) Under $y = 0$ cm. (b) Under $y = 5$ cm. (c) Under $y = 10$ cm.

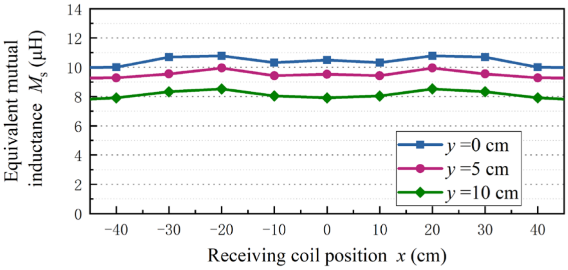

Fig. 13. Simulated equivalent mutual inductance at different receiving coil positions under lateral misalignments.

Fig. 13 shows the simulated equivalent mutual inductance M_s at different receiving coil positions under lateral misalignment. Under $y = 0$ cm, 5 cm, and 10 cm, the fluctuation rates of mutual inductance M_s are ±2%, ±3%, and ±4%, respectively. The results show that the design of bilateral reverse coils reduces the fluctuation in mutual inductance as the receiving coil moves along the transmitting coils under misalignment. However, the overall output power still decreases when there is a lateral misalignment compared with the standard output power. Based on the simulation design, the standard equivalent mutual inductance values under lateral misalignments $y =$ 0 cm, 5 cm, and 10 cm are obtained as: $M_{s\cdot a} = 10.8$ μH, $M_{s\cdot b} = 10.0$ μH, and $M_{s\cdot c} = 8.6$ μH. The optimization process for the quasi-resonant parameters is performed, resulting in $L_f =$

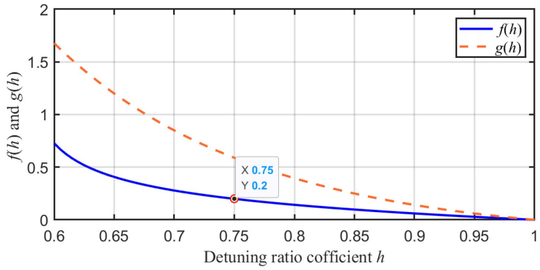

Fig. 14. Function curves of *f*(*h*) and *g*(*h*) with *h* under optimized parameters.

16.7 μH, $L_{ses0} = 21.6\ \mu$H, and $h_1 = 0.75$. Consequently, the optimized quasi-resonant range is (0.75, 1).

To verify the superiority of the variable resistance modeling method for nonresonant *LCC–LCC* topology, a comparative analysis is conducted. Combine with (8) and (13), the resonant angle tangent obtained from solving the conventional EVDWC system with a constant resistance model is

$$\tan\beta = g(h) = \frac{(1-h)[(1-2h)\omega^2 {L^2}_{ses} + R^2]}{h^2\omega L_{ses} R}. \quad (20)$$

Based on the standard output power under resonant configuration, the equivalent resistance of the load *R* is set to 14 Ω. The function curves of *f*(*h*) and *g*(*h*) with the detuning ratio coefficient *h* under the optimized parameter configuration are plotted in Fig. 14. The calculation results show that the parameter optimization results obtained by using the modeling method in this article can achieve a larger range of detuning ratio coefficients under good ZVS conditions.

D. Optimization of the Secondary-Side Integrated Coil

To enhance the compactness of the receiver and broaden the circuit parameter selection corresponding to quasi-resonant range, further optimization of the secondary-side integrated inductor coil is conducted. The result of the equivalent inductance L_{ses} with side length l_6 and turns n_{w4} as variables is shown in Fig. 15(a). After the first judgment, three optimization result combinations will be obtained in sequence, namely: 160 mm with 6, 180 mm with 5, and 200 mm with 4. The lower limit of the corresponding detuning ratio coefficient and the maximum value of cross mutual inductance are calculated, as shown in Fig. 15(b) and Fig. 15(c), respectively. The shaded ranges are invalid regions, and the parameters within these ranges do not meet the corresponding expected criteria. The first result satisfies both constraints simultaneously. In the course of the optimization process, the first outcome concurrently fulfills all the stipulated optimization criteria and is, therefore, obtained as the definitive solution for the integrated inductor coil. Therefore, the size of the secondary-side integrated inductor coil is designed as "160 mm ∗ 160 mm ∗ 5 mm." The turns n_{w4} is designed as 6.

IV. VALIDATION

To validate the theoretical analysis presented in this article about the integrated optimization method to suppress the power fluctuation under lateral misalignment, a 4.5-kW power-level EVDWC system prototype has been constructed. Simulations and experiments are performed to verify the feasibility of the proposed method.

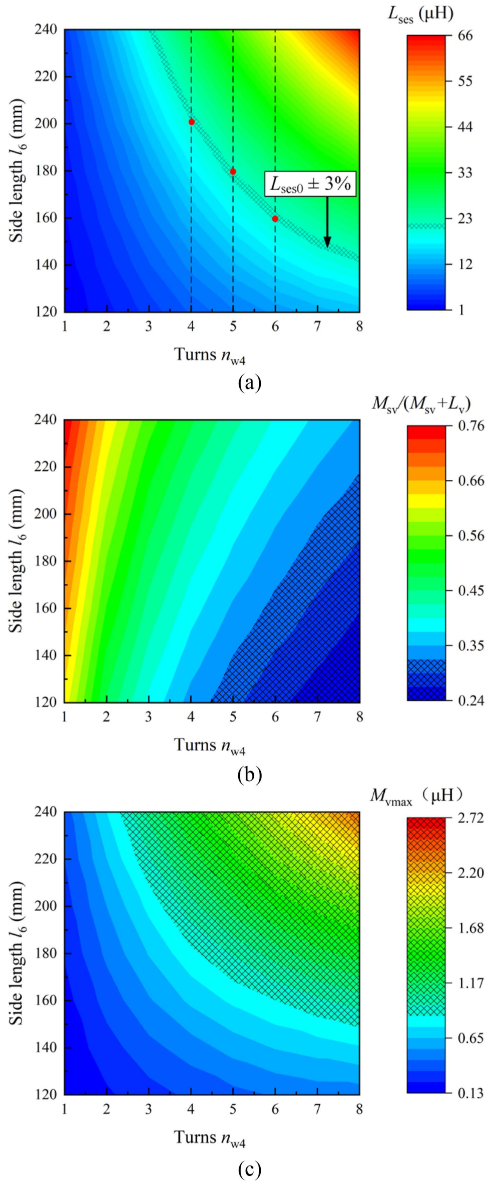

Fig. 15. Results of the secondary-side integrated inductor parameters affected by the turns n_{w4} and length l_6. (a) Optimization results of equivalent inductance L_{ses}. (b) Optimization results of the lower limit of the detuning ratio coefficient configuration. (c) Optimization results of the cross mutual inductance between the integrated inductor and primary coils.

A. Simulation Analysis

The system simulation model corresponding to Fig. 5 is built based on the simulation parameters in Table II. The inverter voltage and battery voltage are set to 400 V and 250 V, respectively. The simulated inverter output waveforms under different receiving coil positions and lateral misalignments are shown in Fig. 16. u_i is the output voltage of the inverter, i_1 and i_2 are the inverter output branch currents corresponding to the two transmitters,

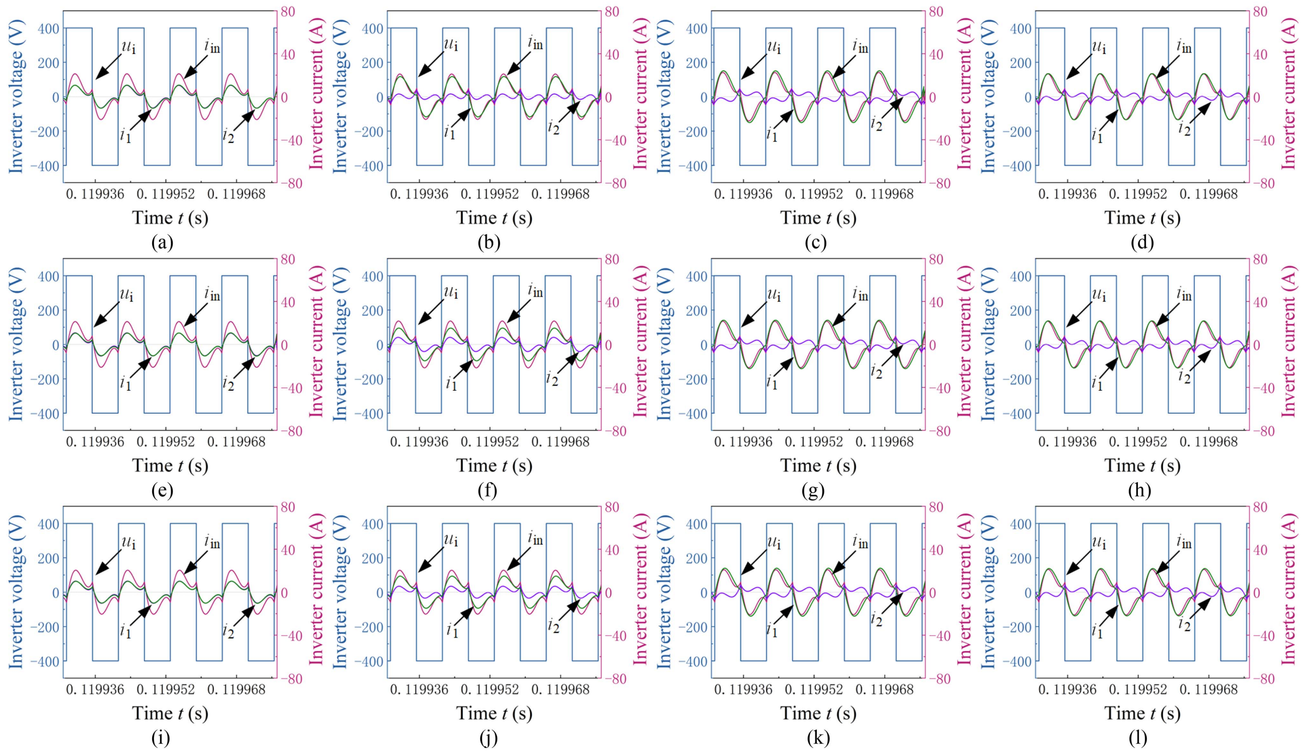

Fig. 16. Simulated inverter output waveforms under different receiving coil positions and lateral misalignments. (a) $y = 0$ cm, $x = 0$ cm, and $h_s = 1(C_v = 243$ nF). (b) $y = 0$ cm, $x = 15$ cm, and $h_s = 1(C_v = 243$ nF). (c) $y = 0$ cm, $x = 30$ cm, and $h_s = 1(C_v = 243$ nF). (d) $y = 0$ cm, $x = 45$ cm, and $h_s = 1(C_v = 243$ nF). (e) $y = 5$ cm, $x = 0$ cm, and $h_s = 0.93(C_v = 272$ nF). (f) $y = 5$ cm, $x = 15$ cm, and $h_s = 0.93(C_v = 272$ nF). (g) $y = 5$ cm, $x = 30$ cm, and $h_s = 0.93(C_v = 272$ nF). (h) $y = 5$ cm, $x = 45$ cm, and $h_s = 0.93(C_v = 272$ nF). (i) $y = 10$ cm, $x = 0$ cm, and $h_s = 0.83(C_v = 327$ nF). (j) $y = 10$ cm, $x = 15$ cm, and $h_s = 0.83(C_v = 327$ nF). (k) $y = 10$ cm, $x = 30$ cm, and $h_s = 0.83(C_v = 327$ nF). (l) $y = 10$ cm, $x = 45$ cm, and $h_s = 0.83(C_v = 327$ nF).

TABLE II
SIMULATED COUPLER PARAMETERS AND RESONANCE PARAMETERS

Symbol	Parameters	Value
f	Resonant frequency	85 kHz
L_1, L_2	Primary-side compensation inductor	42.0 μH
L_v	Secondary-side integrated inductor coil	14.5 μH
L_{p1}, L_{p2}	Transmitting coil	86.3 μH
L_{r1}, L_{r2}	Primary-side integrated bilateral reverse coil	32.1 μH
L_s	Receiving coil	95.0 μH
C_1, C_2	Primary-side compensation capacitor	138.6 nF
C_{f1}, C_{f2}	Primary-side compensation capacitor	209.9 nF
C_{p1}, C_{p2}	Primary-side compensation capacitor	43.5 nF
C_s	Secondary-side compensation capacitor	43.6 nF
C_o	Filter capacitor	40.0 μF
R_1, R_2, R_4, R_5, R_8, R_9	Internal resistances	0.04 Ω
R_3, R_6, R_7	Internal resistances	0.08 Ω

and i_{in} is the total superimposed current of i_1 and i_2. And h_s is the detuning ratio coefficient in simulation. The simulation results indicate that the optimized BRI system operates under weakly inductive ZVS conditions across various receiving coil positions, utilizing three quasi-resonant parameters' configurations.

The simulation results of the output power and efficiency at different receiving coil positions with the internal resistances are shown in Fig. 17. Under $y = 0$ cm, when the receiving coil moves from −45 to 45 cm, the output power is between 4.41 and 4.58 kW, with an average output power of 4.51 kW and a power fluctuation of less than ±3%. The maximum efficiency of dc–dc reaches 92.8%. Under $y = 5$ cm, when the receiving coil moves from −45 to 45 cm, the output power is between 4.41 and 4.65 kW, with an average output power of 4.5 kW and a power fluctuation of less than ±4%. The maximum efficiency of dc–dc reaches 92.6%. Under $y = 10$ cm, when the receiving coil moves from −45 to 45 cm, the output power is between 4.36 and 4.66 kW, with an average output power of 4.52 kW and a power fluctuation of less than ±5%. The maximum efficiency of dc–dc reaches 92.0%. The results show that under different lateral misalignments, the simulated output power during the receiving coil moving along the transmitting coils is stable and approximately reaches the standard value. The efficiency is high and relatively stable. And the influence characteristics of internal resistances on the output power and efficiency do not change the overall law of the system.

B. Experimental Setup

To verify the correctness of the theoretical analysis and design methods, the experimental coil wound according to the design results in Section III is shown in Fig. 18, and the construction of the entire experimental prototype is shown in Fig. 19. The measured coupler parameters and calculated resonant parameters are shown in Table III.

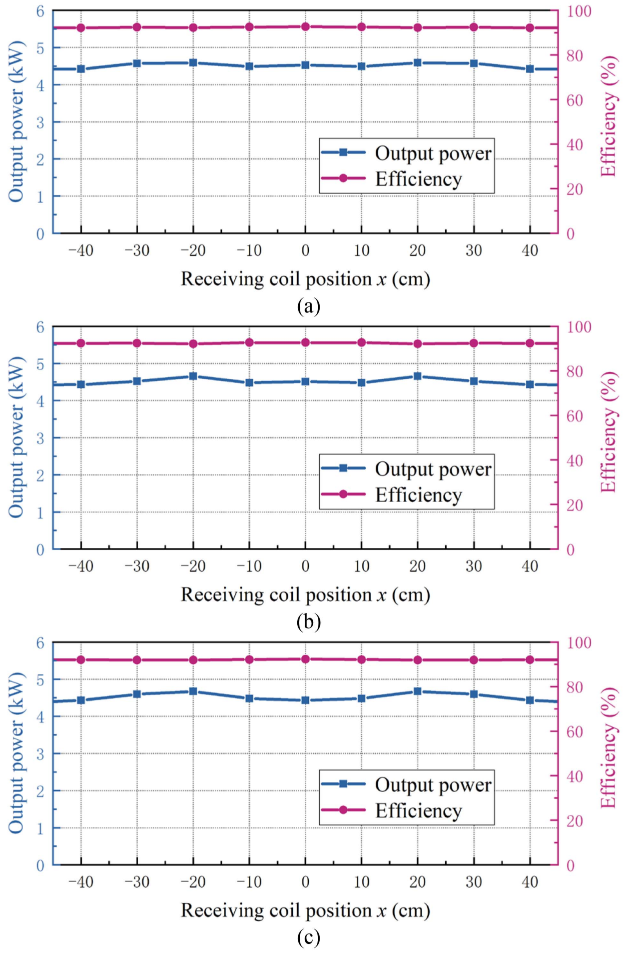

(a)

(b)

(c)

Fig. 17. Simulated output power and efficiency under different lateral misalignments. (a) $y = 0$ cm and $h_s = 1 (C_v = 243$ nF). (b) $y = 5$ cm and $h_s = 0.93 (C_v = 272$ nF). (c) $y = 10$ cm and $h_s = 0.83 (C_v = 327$ nF).

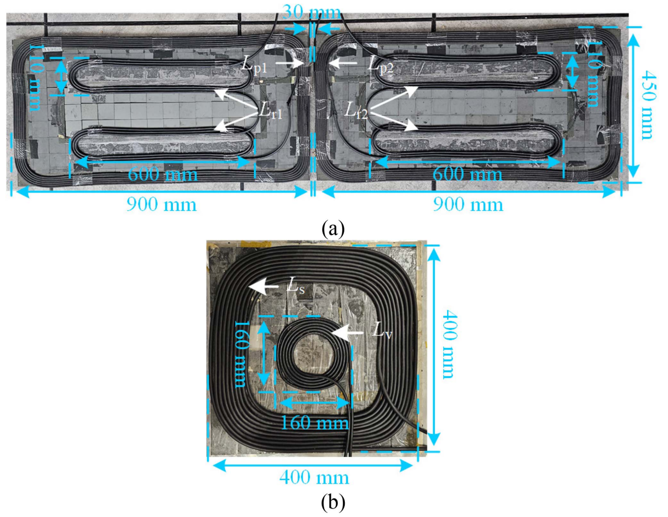

(a)

(b)

Fig. 18. Prototype of the BRI magnetic coupler. (a) Transmitting coils L_{p1} and L_{p2} and integrated reverse coils L_{r1} and L_{r2}. (b) Receiving coil L_s and the secondary-side integrated inductor L_v.

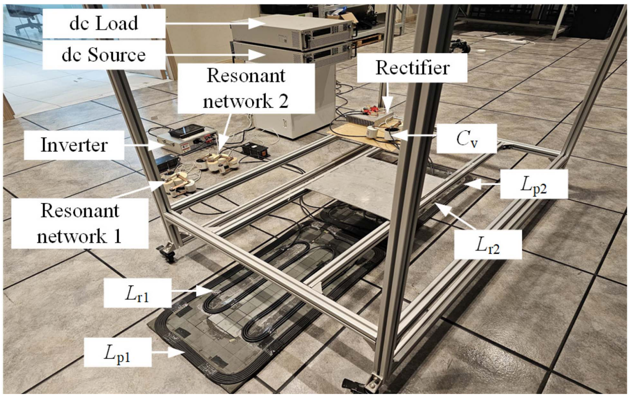

Fig. 19. Prototype of the EVDWC system with BRI magnetic coupler and quasi-resonant parameter configuration.

TABLE III
MEASURED COUPLER PARAMETERS AND RESONANCE PARAMETERS

Symbol	Parameters	Value
f	Resonant frequency	85 kHz
L_1	Primary-side compensation inductor	42.1 μH
L_2	Primary-side compensation inductor	42.0 μH
L_v	Secondary-side integrated inductor coil	14.2 μH
L_{p1}	Transmitting coil	84.3 μH
L_{p2}	Transmitting coil	83.8 μH
L_{r1}	Primary-side integrated reverse coil	30.3 μH
L_{r2}	Primary-side integrated reverse coil	30.7 μH
L_s	Receiving coil	93.4 μH
C_1	Primary-side compensation capacitor	140.1 nF
C_2	Primary-side compensation capacitor	139.7 nF
C_{f1}	Primary-side compensation capacitor	207.5 nF
C_{f2}	Primary-side compensation capacitor	207.2 nF
C_{p1}	Primary-side compensation capacitor	45.9 nF
C_{p2}	Primary-side compensation capacitor	45.7 nF
C_s	Secondary-side compensation capacitor	44.5 nF
C_o	Filter capacitor	40.0 μF

At the input, a dc power supply and a high-power inverter are used to provide 400-V dc power to the resonant circuit. The inverter's switching transistor utilizes a CREE silicon carbide MOSFET (C2M0025120D) with an internal resistance of 25 mΩ to minimize power loss. The pulsewidth modulation (PWM) control signal for the MOSFET is generated by the control chip TMS320F28335, operating at a fixed frequency of 85 kHz. Both transmitters are identical and share a full-bridge inverter. At the output, CREE C3D20060D diodes are used to form the rectifier to deliver dc to the EA-CPS-8080 electronic load, which has an output voltage set at 250 V. The coils are wound with 1000 strands of AWG 38 Litz wire, and the magnetic material PC95 is used to construct the magnetic core board. The capacitor model is Mentronix MLC-R high-voltage resonant capacitor. This capacitor features high-frequency low-loss characteristics, excellent temperature stability, and precise resonant behavior, making it suitable for high-frequency resonant circuit design.

TABLE IV
COMPARISON BETWEEN THE MEASURED AND SIMULATED PARAMETERS

Symbol	Simulated value	Measured value	Error rate
L_{v}	14.5 μH	14.2 μH	2%
M_{sv}	7.2 μH	7.0 μH	3%
L_{ses}	21.6 μH	21.2 μH	2%
$M_{\mathrm{s\_a}}$	10.8 μH	10.5 μH	3%
$M_{\mathrm{s\_b}}$	10.0 μH	9.7 μH	3%
$M_{\mathrm{s\_c}}$	8.6 μH	8.4 μH	2%
M_{vmax}	0.8 μH	0.76 μH	5%

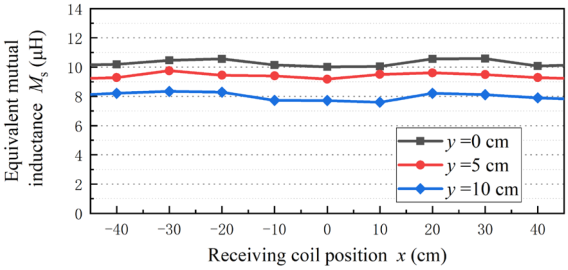

Fig. 20. Equivalent mutual inductance calculated by measured parameters at different receiving coil positions under lateral misalignments.

C. Comparison of Experimental and Simulated Parameters

The comparison between the measured and simulated results of key optimization parameters is shown in Table IV. Differences exist between the measured and simulated parameters due to fabrication errors in the prototype's manufacturing process. The calculated error rate of key parameters shows that the differences in parameters are minimal and acceptable. Meanwhile, the equivalent mutual inductance M_s is calculated using the measured mutual inductance data at various positions of the receiving coil under lateral misalignments, as plotted in Fig. 20. Under $y = 0$ cm, 5 cm, and 10 cm, the fluctuation rates of mutual inductance M_s are ±3%, ±4%, and ±5%, respectively. Compared with the simulation results in Fig. 13, although there are slight differences, the pattern of the total equivalent mutual inductance M_s changes with the position of the receiving coil under different lateral misalignments is approximately consistent. Therefore, the experimental prototype meets the requirements of the method proposed in this article for suppressing the power fluctuation under lateral misalignments.

D. Experimental Results

The output waveforms of the inverter during the movement of the receiving coil are measured under different lateral misalignments, as shown in Fig. 21. Similarly, u_i is the output voltage of the inverter, i_1 and i_2 are the inverter output branch currents corresponding to the two transmitters, and i_{in} is the total superimposed current of i_1 and i_2. And h_e is the detuning ratio coefficient in the experiment. Under $y = 0$ cm, configure $h_e = 1$ ($C_v = 247$ nF) to achieve standard power output without lateral misalignment, with a resonant angle tangent value of 0.02. Under $y = 5$ cm, configure $h_e = 0.93$ ($C_v = 276$ nF), and the resonant angle tangent value is 0.06. Under $y = 10$ cm, configure $h_e = 0.83$ ($C_v = 330$ nF), and the resonant angle tangent value is 0.12. The experimental results indicate that the system can achieve an efficient ZVS working state through parameter configuration within the corresponding quasi-resonant range at $y = 0$ cm, 5 cm, and 10 cm.

Fig. 22 demonstrates the output power and efficiency when the receiving coil is above the transmitting coils under various lateral misalignments. The results indicate that the proposed method can effectively suppress output power fluctuation even with 10-cm lateral misalignment. Through parameter configuration within the quasi-resonant range, the average output power is increased to the standard value. Under $y = 0$ cm, when the receiving coil moves from -45 to 45 cm, the output power is between 4.51 and 4.77 kW, with an average output power of 4.67 kW and a power fluctuation of less than ±4%. The maximum efficiency of dc–dc reaches 92.6%. Under $y = 5$ cm, when the receiving coil moves from -45 to 45 cm, the output power is between 4.38 and 4.71 kW, with an average output power of 4.51 kW and a power fluctuation of less than ±5%. The maximum efficiency of dc–dc reaches 92.2%. Under $y = 10$ cm, when the receiving coil moves from -45 to 45 cm, the output power is between 4.28 and 4.75 kW, with an average output power of 4.54 kW and a power fluctuation of less than ±6%. The maximum efficiency of dc–dc reaches 91.5%. Comparing Fig. 22 with Fig. 17, the calculated output power fluctuation in the experimental results is slightly higher than the simulation results, with an error of about 1%. However, the optimization effect remains quite effective. In addition, the effectiveness of theoretical analysis ignoring internal resistance and M_v has been verified.

V. DISCUSSION

A. Discussion of Feature

To overcome the issue of output power fluctuation in EVDWC systems caused by simultaneous lateral misalignment and transmitting coil switching, a novel magnetic integrated and quasi-resonant parameter optimization method is proposed. The effect of enhancing output power capability through a single parameter while maintaining ZVS operation is achieved. By minimizing mutual inductance fluctuation during transmitting coil switching under lateral misalignment and compensating power drops caused by lateral misalignment, the power stability of the EVDWC system is achieved.

The comparison between this article with the latest related research is given in Table V. First, in [1], [5], [10], [20], and [21], the issue of output power fluctuation caused solely by transmitting coil switching was addressed, without considering the effect of lateral misalignments. In [26], although the simulation and experimental sections verified the effectiveness of suppressing output power fluctuation under a 6-cm lateral misalignment, the lateral misalignment was not considered in theoretical analysis. Existing methods lack analysis for suppressing output power fluctuation during EV movement under lateral misalignments. Second, in [1], [5], [10], [20], and [26], those magnetic couplers have specific shapes or structures, which make the compatibility between the transmitting coil and the receiving coil poor. In [21],

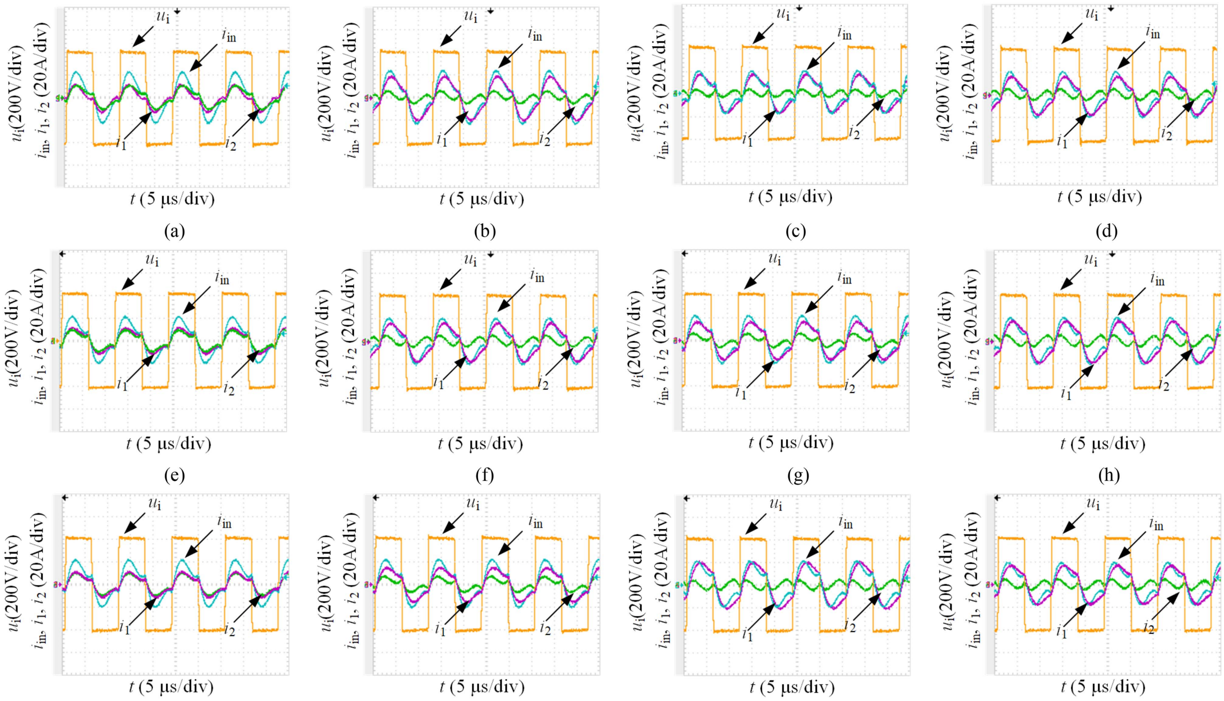

(a) (b) (c) (d) (e) (f) (g) (h) (i) (j) (k) (l)

Fig. 21. Inverter output waveforms under different receiving coil positions and lateral misalignments. (a) $y = 0$ cm, $x = 0$ cm, and $h_e = 1(C_v = 247$ nF). (b) $y = 0$ cm, $x = 15$ cm, and $h_e = 1(C_v = 247$ nF). (c) $y = 0$ cm, $x = 30$ cm, and $h_e = 1(C_v = 247$ nF). (d) $y = 0$ cm, $x = 45$ cm, and $h_e = 1(C_v = 247$ nF). (e) $y = 5$ cm, $x = 0$ cm, and $h_e = 0.93(C_v = 276$ nF). (f) $y = 5$ cm, $x = 15$ cm, and $h_e = 0.93(C_v = 276$ nF). (g) $y = 5$ cm, $x = 30$ cm, and $h_e = 0.93(C_v = 276$ nF). (h) $y = 5$ cm, $x = 45$ cm, and $h_e = 0.93(C_v = 276$ nF). (i) $y = 10$ cm, $x = 0$ cm, and $h_e = 0.83(C_v = 330$ nF). (j) $y = 10$ cm, $x = 15$ cm, and $h_e = 0.83(C_v = 330$ nF). (k) $y = 10$ cm, $x = 30$ cm, and $h_e = 0.83(C_v = 330$ nF). (l) $y = 10$ cm, $x = 45$ cm, and $h_e = 0.83(C_v = 330$ nF).

TABLE V
COMPARISON BETWEEN THE LATEST RELATED RESEARCH AND THIS WORK

Ref	Maximum Efficiency	Power Capability	Maximum Coupling Coefficient	Coupler Structure	Modeling of Battery Load	Maximum Misalignment in Moving Direction	Maximum Lateral Misalignment	Compatibility of Tx with Rxs	Dynamic Output Voltage (V)/Power Fluctuation (P)
[1]	91.70%	0.25 kW	0.14	Tx: I-shaped solenoid Rx: Q and solenoid	Constant resistance	9.5 cm	/	Low	V: ± 2.8% (y = 0 cm)
[5]	93.07%	0.94 kW	0.22	Tx: Q, Rx: TDC	Constant resistance	46 cm	/	Medium	V: ± 3.49% (y = 0 cm)
[10]	95.30%	1.30 kW	0.27	Tx: Q, Rx: DD	Constant resistance	25 cm	/	Medium	P: ± 3.5% (y = 0 cm)
[20]	92.30%	12.00 kW	0.11	Tx: DD&Q, Rx: DD&Q	Constant resistance	75 cm	/	Medium	P: ± 4% (y = 0 cm)
[21]	91.00%	0.07 kW	0.11	Tx and Rx: Q	Constant resistance	20 cm	/	High	P: ± 7.4% (y = 0 cm)
[26]	91.04%	3.30 kW	0.10	Tx: SBP, Rx: X	Constant resistance	27 cm	6 cm	Low	V: ± 3% (y = 0 cm) V: ± 3.47% (y = 6 cm)
This work	92.60%	4.50 kW	0.12	Tx & Rx: Q	Variable resistance	45 cm	10 cm	High	P: ± 4% (y = 0 cm) P: ± 5% (y = 5 cm) P: ± 6% (y = 10 cm)

although the applicability of the method is strong, the effectiveness still needs to be improved. In this article, two sets of unipolar coils are integrated based on the original conventional unipolar transmitting and receiving coils, which makes the method more versatile. For a given initial magnetic coupler, an improved BRI magnetic coupler can be designed based on the optimization method. In addition, in the relevant literature, the constant resistance model of battery is adopted in circuit analysis. In this article, a parameter optimization method for quasi-resonant *LCC–LCC* topology is proposed using a variable resistance load model under the battery voltage constraint condition, achieving its output power capability improvement while maintaining an optimal weak inductive ZVS condition. By optimizing the quasi-resonant parameters, the power output capability of the system is effectively enhanced while maintaining approximate resonance. Thus, the overall improvement in output power is achieved under lateral misalignment. The proposed method is universal and has no special requirements for the coupling coefficient.

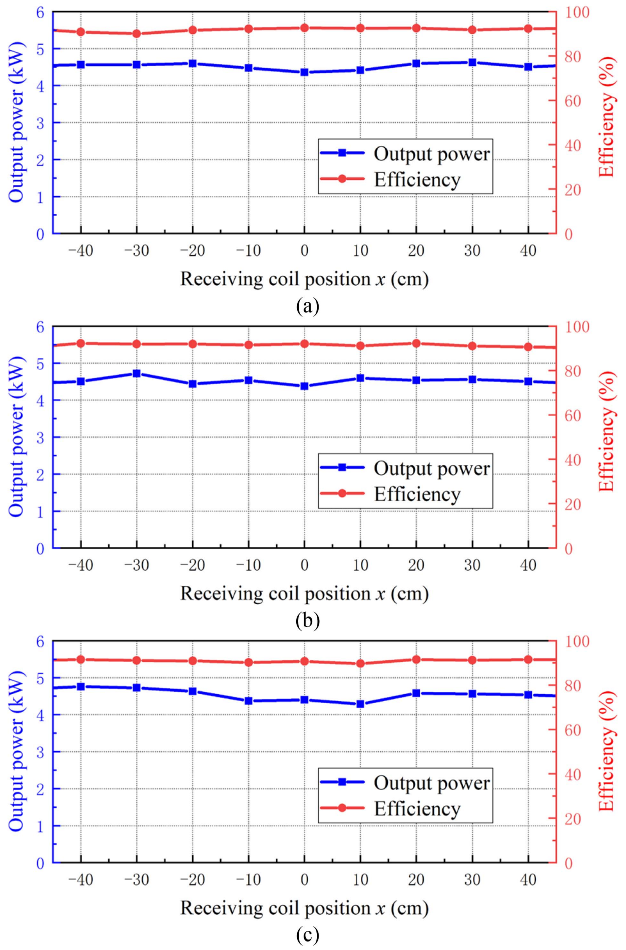

(a)

(b)

(c)

Fig. 22. Experimental output power and efficiency under different lateral misalignments. (a) $y = 0$ cm and $h_e = 1(C_v = 247$ nF). (b) $y = 5$ cm and $h_e = 0.93(C_v = 276$ nF). (c) $y = 10$ cm and $h_e = 0.83(C_v = 330$ nF).

B. Discussion of Practical Application

In this article, adjusting the compensation capacitor C_v is just an implementation step to validate the theoretical analysis of the proposed quasi-resonant parameter optimization method. C_v is used to adjust the detuning ratio coefficient h under different lateral misalignment distances, but in practical situations, the real-time requirements for parameter adjustment are not high. This is because lateral misalignments in EVDWC systems typically occur gradually, and adjustments are required in seconds. For the EVDWC system working at 85 kHz, even with EV speeds of 60 km/h, the lateral alignment state changes at a rate of seconds or longer, making parameter adjustment feasible. Adjustable capacitors controlled by PWM [27], [28], [29] or dc voltage control [30] have been proven to achieve adjustment times in the millisecond range, sufficient for the gradual misalignment scenarios.

In addition, a single inverter drives two *LCC* resonant network topologies simultaneously to reduce cost and complexity [31], [32]. There may be slight parallel circulating currents in practical operation. However, due to the impedance characteristics under the resonant configuration of the primary *LCC* topologies [33], [34], the generated circulating current is small and will not cause serious efficiency losses in the system. It has no essential impact on the theoretical analysis, which is universal for both single/dual inverter topologies.

The proposed method realizes the suppression of power fluctuation during the EV movement under lateral misalignment. In general, the reverse coil means that more copper will be used at the same power level, resulting in a slight decrease in efficiency at a single operating point. However, to achieve the same power supply across the entire road for the overall performance of the EVDWC system, the method ingeniously reduces or even eliminates this inherent defect while suppressing power fluctuation.

VI. CONCLUSION

In this article, an integrated optimization method based on BRI magnetic coupler and quasi-resonant *LCC–LCC* topology is proposed to address the output power fluctuation issue during EV moving under lateral misalignment. A bilateral reverse coil is integrated into the transmitter, and detailed design and optimization methods are provided. The parameter optimization method for quasi-resonant *LCC–LCC* topology is proposed using a variable resistance load model under the battery voltage constraint condition, achieving its output power capability improvement while maintaining an optimal weak inductive ZVS condition. The selection of circuit parameters corresponding to the quasi-resonant range is broadened by the integrated inductor. The proposed method is validated by simulation and experiment with a 4.5-kW power level. The results show that the system maintains stable power transfer within a 10-cm lateral misalignment range, achieving an efficiency above 91.5%. Experimental results have shown that under $y = 0$ cm, 5 cm, and 10 cm, the output power fluctuation rates are ±4%, ±5%, and ±6%. The analysis method in this article has been validated through the comparison between simulation and experiment. The simulation results are slightly better, with an error rate of 1%.

REFERENCES

[1] Y. Zhang, H. Zhou, R. Xie, X. Mao, X. Chen, and Z. Li, “A smooth-output dynamic wireless charging system for automated guided vehicles with dual-receiver magnetic coupler,” *IEEE Trans. Power Electron.*, vol. 40, no. 4, pp. 4711–4715, Apr. 2025.

[2] F. Zhao, S. Cui, C. C. Chan, and C. Zhu, “Modeling of high-efficiency nonsalient pole transmitter in high-power dynamic wireless charging system for electric vehicles,” *IEEE Trans. Power Electron.*, vol. 39, no. 7, pp. 8872–8882, Jul. 2024.

[3] M. Zhang, Z. Liu, and H. Su, “Optimal output regulation for EV dynamic wireless charging system via internal model-based control,” *IEEE Trans. Ind. Electron.*, vol. 71, no. 10, pp. 13031–13041, Oct. 2024.

[4] T. Newbolt, P. Mandal, H. Wang, and R. Zane, “Sustainability of dynamic wireless power transfer roadway for in-motion electric vehicle charging,” *IEEE Trans. Transp. Electron.*, vol. 10, no. 1, pp. 1347–1362, Mar. 2024.

[5] H. Zhou, Z. Shen, Y. Wu, X. Chen, and Y. Zhang, “A stable dynamic electric vehicle wireless charging system based on triple decoupling receiving coils and a novel triple-diode rectifier,” *IEEE Trans. Ind. Electron.*, vol. 71, no. 10, pp. 12011–12018, Oct. 2024.

[6] M. Zhang, Z. Liu, and H. Su, “Robust adaptive output regulation for EV dynamic wireless charging system with sinusoidal disturbance of unknown frequency,” *IEEE Trans. Ind. Electron.*, vol. 71, no. 7, pp. 7301–7311, Jul. 2024.

[7] S. Li, L. Wang, Y. Guo, C. Tao, and L. Ji, “Power stabilization with double transmitting coils and T-type compensation network for dynamic wireless charging of EV,” *IEEE J. Emerg. Sel. Topics Power Electron.*, vol. 8, no. 2, pp. 1801–1812, Jun. 2020.

[8] C. Zhu et al., “A magnetic field concentration enhanced I-shaped transmitter for DWPT system to achieve low power fluctuation,” *IEEE Trans. Power Electron.*, vol. 39, no. 1, pp. 1690–1700, Jan. 2024.

[9] J. Liu, Z. Liu, W. Chen, X. Sun, and H. Su, “An optimized coil array and passivity-based control for receiving side multilevel connected DC-DC converter of dynamic wireless charging,” *IEEE Trans. Veh. Technol.*, vol. 71, no. 4, pp. 3715–3726, Apr. 2022.

[10] Y. Zhang, H. Zhou, Z. Shen, R. Xie, X. Chen, and X. Mao, “An interoperable dynamic wireless charging system with stable output based on a self-adaptive two-pole receiver,” *IEEE Trans. Power Electron.*, vol. 39, no. 10, pp. 11943–11947, Oct. 2024.

[11] J. Liu, Z. Liu, and H. Su, “Passivity-based PI control for receiver side of dynamic wireless charging system in electric vehicles,” *IEEE Trans. Ind. Electron.*, vol. 69, no. 1, pp. 783–794, Jan. 2022.

[12] T. Ma, C. Q. Jiang, C. Chen, Y. Wang, J. Geng, and C. K. Tse, “A low computational burden model predictive control for dynamic wireless charging,” *IEEE Trans. Ind. Electron.*, vol. 71, no. 9, pp. 10402–10413, Sep. 2024.

[13] Q. Zhang, X. Zhang, W. Li, T. Hu, Y. Wang, and S. Shen, “New control method for receiver-side DC–DC converter with large stability margin and fluctuation suppression toward DWPT system,” *IEEE Trans. Ind. Electron.*, vol. 70, no. 8, pp. 7944–7954, Aug. 2023.

[14] K. Chen, J. Pan, Y. Yang, and K. W. E. Cheng, “Stability improvement and overshoot damping of SS-compensated EV wireless charging systems with user-end buck converters,” *IEEE Trans. Veh. Technol.*, vol. 71, no. 8, pp. 8354–8366, Aug. 2022.

[15] H. Li, Y. Liu, K. Zhou, Z. He, W. Li, and R. Mai, “Uniform power IPT system with three-phase transmitter and bipolar receiver for dynamic charging,” *IEEE Trans. Power Electron.*, vol. 34, no. 3, pp. 2013–2017, Mar. 2019.

[16] B. Song, B. Du, S. Cui, Y. Li, and C. Zhu, “Mechanism analysis of output fluctuation in a three-phase dynamic wireless charging system,” *IEEE Trans. Ind. Electron.*, vol. 69, no. 3, pp. 2252–2264, Mar. 2022.

[17] V.-B. Vu, M. Dahidah, V. Pickert, and V.-T. Phan, “A high-power multiphase wireless dynamic charging system with low output power pulsation for electric vehicles,” *IEEE J. Emerg. Sel. Topics Power Electron.*, vol. 8, no. 4, pp. 3592–3608, Dec. 2020.

[18] H. Feng, T. Cai, S. Duan, J. Zhao, X. Zhang, and C. Chen, “An LCC-compensated resonant converter optimized for robust reaction to large coupling variation in dynamic wireless power transfer,” *IEEE Trans. Ind. Electron.*, vol. 63, no. 10, pp. 6591–6601, Oct. 2016.

[19] W. Xiong, Q. Yu, Z. Liu, L. Zhao, Q. Zhu, and M. Su, “A detuning-repeater-based dynamic wireless charging system with quasi-constant output power and reduced inverter count,” *IEEE Trans. Power Electron.*, vol. 38, no. 1, pp. 1336–1347, Jan. 2023.

[20] K. Shi, C. Tang, H. Long, X. Lv, Z. Wang, and X. Li, “Power fluctuation suppression method for EV dynamic wireless charging system based on integrated magnetic coupler,” *IEEE Trans. Power Electron.*, vol. 37, no. 1, pp. 1118–1131, Jan. 2022.

[21] Z. Li, J. Li, S. Li, Y. Yu, and J. Yi, “Design and optimization of asymmetric and reverse series coil structure for obtaining quasi-constant mutual inductance in dynamic wireless charging system for electric vehicles,” *IEEE Trans. Veh. Technol.*, vol. 71, no. 3, pp. 2560–2572, Mar. 2022.

[22] M. Wu et al., “A compact coupler with integrated multiple decoupled coils for wireless power transfer system and its anti-misalignment control,” *IEEE Trans. Power Electron.*, vol. 37, no. 10, pp. 12814–12827, Oct. 2022.

[23] J. Wang, R. Chen, C. Cai, J. Zhang, and C. Wang, “An onboard magnetic integration-based WPT system for UAV misalignment-tolerant charging with constant current output,” *IEEE Trans. Transp. Electron.*, vol. 9, no. 1, pp. 1973–1984, Mar. 2023.

[24] N. Rasekh, J. Kavianpour, and M. Mirsalim, “A novel integration method for a bipolar receiver pad using LCC compensation topology for wireless power transfer,” *IEEE Trans. Veh. Technol.*, vol. 67, no. 8, pp. 7419–7428, Aug. 2018.

[25] J. Yin, S. Mekhilef, P. Darvish, H. Mokhlis, and T. K. Soon, “A new cross-overlapped decoupling coil structure for EV dynamic inductive wireless charging system,” *IEEE Trans. Ind. Electron.*, vol. 72, no. 2, pp. 1314–1324, Feb. 2025.

[26] L. Cheng, G. Wei, L. Hao, Y. Zhang, and J. Zhang, “A staggered bipolar magnetic coupler for dynamic wireless charging system,” *IEEE Trans. Power Electron.*, vol. 40, no. 7, pp. 10242–10253, Jul. 2025.

[27] K. Song et al., “A control strategy for wireless EV charging system to improve weak coupling output based on variable inductor and capacitor,” *IEEE Trans. Power Electron.*, vol. 37, no. 10, pp. 12853–12864, Oct. 2022.

[28] X. Xie, C. Xie, Y. Li, J. Wang, Y. Du, and L. Li, “Adaptive decoupling between receivers of multireceiver wireless power transfer system using variable switched capacitor,” *IEEE Trans. Transp. Electron.*, vol. 7, no. 4, pp. 2143–2155, Dec. 2021.

[29] R. Matsumoto, T. Fujita, and H. Fujimoto, “Communicationless reactance compensation using PWM-controlled switched capacitors for wireless power transfer,” *IEEE Trans. Power Electron.*, vol. 38, no. 10, pp. 13194–13206, Oct. 2023.

[30] J. Tian and A. P. Hu, “A DC-voltage-controlled variable capacitor for stabilizing the ZVS frequency of a resonant converter for wireless power transfer,” *IEEE Trans. Power Electron.*, vol. 32, no. 3, pp. 2312–2318, Mar. 2017.

[31] Z. Deng et al., “Design of a 60-kW EV dynamic wireless power transfer system with dual transmitters and dual receivers,” *IEEE J. Emerg. Sel. Topics Power Electron.*, vol. 12, no. 1, pp. 316–327, Feb. 2024.

[32] Z. Deng et al., “A method based on vector-summing to reduce output power fluctuation for EV-DWPT system with the passive LC network,” *IEEE Trans. Transp. Electron.*, vol. 11, no. 1, pp. 2133–2145, Feb. 2025.

[33] A. Khoshsaadat and J. S. Moghani, “Fifth-order T-type passive resonant tanks tailored for constant current resonant converters,” *IEEE Trans. Circuits Syst. I, Reg. Papers*, vol. 65, no. 2, pp. 842–853, Feb. 2018.

[34] Y. Chen et al., “A parameter tuning method for a double-sided compensated IPT system with constant-voltage output and efficiency optimization,” *IEEE Trans. Power Electron.*, vol. 38, no. 3, pp. 4124–4139, Mar. 2023.

Ke Shi (Member, IEEE) received the B.E. and Ph.D. degrees from the School of Automation, Chongqing University, Chongqing, China, in 2016 and 2022, respectively.

He is currently a Lecturer with the School of Automation, Chongqing University of Posts and Telecommunications, Chongqing, China. His current research interests include wireless power transfer and power electronics, dynamic wireless charging systems, and magnetic integrated method.

Chunsen Tang (Member, IEEE) received the B.S. and Ph.D. degrees from the School of Automation, Chongqing University, Chongqing, China, in 2004 and 2009, respectively.

In 2008, he was a Research Fellow with the Department of Electrical and Computer Engineering, The University of Auckland, Auckland, New Zealand. In 2009, he joined the School of Automation, Chongqing University, where he is currently a Professor. His current research interests include nonlinear modeling and analysis, intelligent control, and wireless power transfer.

Tianxu Feng (Member, IEEE) received the B.E. degree in automation and the Ph.D. degree in control theory and control engineering from the School of Automation, Chongqing University, Chongqing, China, in 2016, and 2022, respectively.

He is currently an Associate Professor with the School of Automation, Chongqing University of Posts and Telecommunications, Chongqing, China. His current research interests include the wireless power transfer and power electronics.

Peiyue Wang received the B.E. degree in automation from Xidian University, Xi'an, China, in 2015, and the Ph.D. degree in control theory and engineering from Chongqing University, Chongqing, China, in 2021.

He is currently a Lecturer with the School of Automation, Chongqing University of Posts and Telecommunications, Chongqing, China. His current research interests include the wireless power transfer and power electronics.

Jincheng Jiang received the Ph.D. degree in control theory and control engineering from the School of Automation, Chongqing University, Chongqing, China, in 2020.

He is currently a Lecturer with the School of Automation, Chongqing University of Posts and Telecommunications, Chongqing, China. His research interests include wireless power transfer technology and industrial IoT technology.

Jun Wang received the B.E. degree from the Wuchang University of Technology, Wuhan, China, in 2014, the M.S. degree from the Chongqing University of Posts and Telecommunications, Chongqing, China, in 2017, and the Ph.D. degree from Xi'an Jiaotong University, Xi'an, China, in 2020.

He is currently an Associate professor with the College of Automation, Chongqing University of Posts and Telecommunications, Chongqing, China. His main research interests include model predictive control and multienergy flow systems.

Jie Hou (Member, IEEE) received the B.Eng. degree in automation from North Minzu University, Yinchuan, China, in 2010, the M.Eng. degree in control science and engineering from Chongqing University, Chongqing, China, in 2013, and the Ph.D. degree in control theory and control engineering from the Dalian University of Technology, Dalian, China, in 2018.

From 2018 to 2021, he was a Lecturer with the Chongqing University of Posts and Telecommunications, Chongqing, China, where he is currently an Associate Professor. His current research interests include system identification and modeling.

Shuaiyong Li (Senior Member, IEEE) received the B.Sc. degree in applied physics from Xinyang Normal University, Xinyang, China, in 2010, and the Ph.D. degree in instrument science and technology from Chongqing University, Chongqing, China, in 2014.

From 2021 to 2023, he was a Postdoctoral Fellow with Chongqing University. He is currently a Full Professor with the School of Automation, Chongqing University of Posts and Telecommunications, Chongqing, China. He has authored or coauthored more than 60 scientific papers in international journals and conferences. His current research interests include simultaneous localization and mapping, mobile robots, fault diagnosis and remaining useful life prediction, defect detection and safety evaluation, and industrial Internet of Things.